Available online at www.sciencedirect.com
ScienceDirect
Polymer 48 (2007) 5308–5323
polymer
www.elsevier.com/locate/polymer

Structure and properties of polypropylene-based nanocomposites: Effect of PP-*g*-MA to organoclay ratio

Do Hoon Kim [a], Paula D. Fasulo [b], William R. Rodgers [b], Donald R. Paul [a,*]

[a] *Department of Chemical Engineering and Texas Materials Institute, The University of Texas at Austin, TX 78712, USA*
[b] *General Motors Research and Development Center, 30500 Mound Road, Warren, MI 48090, USA*

Received 27 April 2007; received in revised form 6 July 2007; accepted 9 July 2007
Available online 13 July 2007

Abstract

The structure–property relationships of polypropylene (PP)-based nanocomposites prepared by melt processing have been investigated with a main focus on the ratio of polypropylene grafted with maleic anhydride (PP-*g*-MA) to organoclay. The morphological observations by transmission electron microscopy and X-ray diffraction are presented in conjunction with the mechanical, rheological and thermal expansion properties of these nanocomposites. Detailed morphological studies and subsequent quantitative particle analyses for the dispersed clay phase reveal that the aspect ratio of clay particles decreases as the amount of clay increases, and it increases as the amount of PP-*g*-MA increases. The rheological properties suggest that the extent of a percolation network can be enhanced by increasing the number of organoclay particles at a fixed ratio of PP-*g*-MA to organoclay and by increasing the degree of exfoliation at fixed clay content. However, mechanical and thermal expansion behaviors do not improve correspondingly in all cases because of the reduction of matrix properties by PP-*g*-MA. The reduction of the modulus and the increase in the expansion of the polymer matrix caused by the presence of PP-*g*-MA are compared to the prediction of the Chow model. Clearly, the amount of PP-*g*-MA added along with its lower crystallinity are important factors affecting the mechanical and thermal expansion properties of PP-based nanocomposites.

Keywords: Polymer nanocomposites; Polypropylene; PP-*g*-MA

1. Introduction

There has been growing interest in polymer/layered silicate nanocomposites since the first synthesis of nylon/clay nanocomposites via in situ polymerization [1–4]. Layered silicates can impart high levels of reinforcement to polymers at low concentrations which makes them attractive for replacement of conventional fillers in many applications. The focus of most industrial research and development has been on formation of nanocomposites by melt mixing or compounding processes because this is generally more attractive than in situ polymerization due to better commercial feasibility and lower cost [3]. Recent studies have shown that organically modified clays can be efficiently exfoliated in polar polymers like polyamides using appropriate melt processing techniques and conditions [5–7].

However, unlike polyamides, the more commonly used polyolefins, like polypropylene (PP) or polyethylene (PE), do not include any polar groups and do not readily lead to high levels of dispersion of the silicate layers. Since the Toyota group reported formation of PP/clay hybrid composites by direct melt mixing of organoclays based on montmorillonite (MMT) with PP grafted with maleic anhydride (PP-*g*-MA) or hydroxyl groups as an additive to facilitate exfoliation and enhanced properties [8–10], PP/clay nanocomposites have been widely investigated [11–26]. It is believed that the polar character of the anhydride causes an affinity for the silicate surface such that the maleated polypropylene can serve as a compatibilizer between the matrix and filler. This approach has been well developed for polypropylene-based systems;

* Corresponding author. Tel.: +1 512 471 5392; fax: +1 512 471 0542.
E-mail address: drp@che.utexas.edu (D.R. Paul).

0032-3861/$ - see front matter © 2007 Elsevier Ltd. All rights reserved.
doi:10.1016/j.polymer.2007.07.011

however, only a few studies have reported how the ratio of PP-*g*-MA to organoclay affects morphology and the related performance of PP-based nanocomposites [16,22].

The objective of this study is to explore in depth how the ratio of PP-*g*-MA to organoclay affects the structure–property relations of PP-based nanocomposites. Detailed morphological analyses are presented and related to mechanical, thermal and rheological properties. In addition, theoretical model predictions are compared to the experimental thermal and mechanical behaviors of these materials.

2. Experimental

2.1. Materials and composite preparation

Nanocomposites were formed by melt compounding mixtures of a PP (melt index = 37 g/10 min, 230 °C), a polypropylene-grafted maleic anhydride (PP-*g*-MA, MA content = 1.0 wt%) and an organoclay (di-methyl, dehydrogenated tallow-montmorillonite, MMT). Compounding was carried out using a Haake co-rotating twin screw extruder (length = 305 mm, L/D = 10) set at a barrel temperature of 170 °C (feed), a die temperature of 190 °C, a screw speed of 280 rpm, and a feed rate of 1 kg/h. Three ratios of PP-*g*-MA to organoclay (0.5, 1.0 and 2.0) were chosen to explore the effect on PP/PP-*g*-MA nanocomposites at fixed organoclay contents of 1, 3, 5 and 7 wt%, irrespectively.

Extruded nanocomposite pellets were dried and then injection molded into standard tensile bars (ASTM D638, Type I) and Izod bars (ASTM D256) in an Arburg Allrounder 305-210-700 injection molding machine using a barrel temperature of 180 °C (feed) to 220 °C (die), a mold temperature of 40 °C, an injection pressure of 35 bar, and a holding pressure of 35 bar. The amount of montmorillonite (MMT) in each extruded batch was determined by placing the central portion of a tensile bar or Izod bar in a furnace at 900 °C for 45 min and weighing the remaining MMT ash with appropriate correction for loss of structural water during incineration.

2.2. Morphology characterization

Thin sections for transmission electron microscopy (TEM) analysis were microtomed from the central and skin regions of an Izod bar; the cuts were made parallel and perpendicular to the flow direction ca. 3–4 cm away from the far end of a 13 cm Izod bar and halfway between the top and bottom surfaces of the bar. These sections were viewed in the three orthogonal directions, flow direction (FD), transverse direction (TD), and normal direction (ND). The related nomenclature can be found elsewhere [27–29]. TEM image analyses were made on a view observed parallel to the transverse direction, or TD (FD–ND plane) in this paper; the morphologies viewed parallel to the flow direction, or FD (TD–ND plane), and parallel to the normal direction, or ND (FD–TD plane), will be presented in subsequent papers. Ultra-thin sections ranging from 50 to 70 nm in thickness were cryogenically cut with a diamond knife at temperatures of −65 °C for the specimen and −58 °C for the knife using an RMC PowerTome XL ultramicrotome. Sections were collected on 300 mesh copper TEM grids and subsequently dried with filter paper. The sections were examined by TEM using a JEOL 2010F TEM with a LaB_6 filament operating at an accelerating voltage of 120 kV.

Wide angle X-ray scans (WAXS) were made using a Scintag XDS 2000 diffractometer in the reflection mode using an incident X-ray wavelength of 1.542 Å at a scan rate of 1.0°/min over the range of $2\theta = 1-30°$. X-ray analyses were performed at room temperature on as-molded specimens. The Izod specimens were oriented such that the incident beam reflected off the transverse face.

2.3. Rheological properties

A Rheometrics Mechanical Spectrometer (RMS 800) was used to measure the rheological characteristics of the PP-based nanocomposites using the parallel fixture. All the rheological measurements were carried out at a fixed temperature of 180 °C under a nitrogen gas flow. Strain sweep tests were carried out for each sample to ensure that the strain used is within the linear viscoelastic range. Frequency sweep tests were made over a range of 0.1–200 rad/s at strains of 1–5%, which is within the linear region for each sample. Specimens for rheological testing were molded in a hot press (Carver, CH 4386) at 180 °C for 5 min. The molded samples were disc shaped with a diameter of 25 mm and 1 mm thickness.

2.4. Mechanical properties

Stress–strain analyses were performed according to ASTM D638 using an Instron model 1137 upgraded for computerized data acquisition. Specimen modulus was determined using an extensometer at a crosshead speed of 0.51 cm/min. Yield strength was also determined at a speed of 0.51 cm/min. Tensile property values reported here represent an average from measurements on at least five specimens.

Notched Izod impact tests were performed at room temperature using a TMI Izod tester (6.8 J hammer and 3.5 m/s impact velocity) according to ASTM D256. Property values reported here represent an average from at least five specimens.

2.5. Thermal expansion properties

Thermal expansion tests were conducted according to ASTM D696 using a Perkin–Elmer thermomechanical analyzer (TMA 7). Rectangular specimens were prepared from the central region of Izod bars. The dimensions of the specimens were as follows: thickness = 3.2 mm, width = 6.4 mm, and height = 12.7 mm. Thermal expansion measurements were mainly made in the flow direction (FD) in this work. Each specimen was held at −40 °C for 5 min, followed by heating at a rate of 5 °C/min to 125 °C and subsequently held for 30 min, then quenched to room temperature. In order to assess both reversible and non-reversible effects, each specimen was stored at room temperature for at least 24 h after the

first heating and then reheated at a rate of 5 °C/min to 125 °C. All measurements were done in a nitrogen atmosphere.

3. Results and discussion

3.1. Morphology characterization by TEM and WAXS

As mentioned earlier, the lack of polar groups in PP makes it difficult to achieve exfoliation of the organoclay; thus, PP-*g*-MA is used to aid the dispersion of silicate platelets in the PP matrix. Generally, the aspect ratio of clay particles, i.e., particle length/particle thickness, is one of the important factors that determine the reinforcement efficiency of clay nanocomposites [27–30]. Aspect ratio can be estimated from careful analyses of TEM images as shown earlier for highly exfoliated polyamide-based systems [27–29,36]. More recently, similar analyses have been described for less well exfoliated nanocomposites [14,30–32] like those based on PP. In this study, we report particle analyses that show the effects of the amount of clay at a fixed ratio of PP-*g*-MA and the effects of the amount of PP-*g*-MA at fixed clay content.

Figs. 1 and 2 show representative TEM images for various clay contents and ratios of PP-*g*-MA to organoclay. All views were taken parallel to the transverse direction, TD, of the injection molded bars. The typical aggregates of MMT platelets were shown when the formation contains no PP-*g*-MA. Even though the number of particles increases as the MMT concentration increases, the particles remain as large aggregates or tactoids. When PP-*g*-MA is added to the PP/organoclay composites, better dispersion of the clay is obtained as can be seen in the TEM images of Fig. 2 where the ratio of PP-*g*-MA to organoclay goes from 0.5 to 2.0 at a fixed content of MMT (5 wt%). As shown in these TEM micrographs, these nanocomposites have a mixed morphological structure, i.e., a combination of tactoids and more exfoliated particles. The degree of exfoliation clearly increases as the ratio of PP-*g*-MA/organoclay increases irrespective of the total clay content. The alignment of clay platelets in the flow direction and the degree

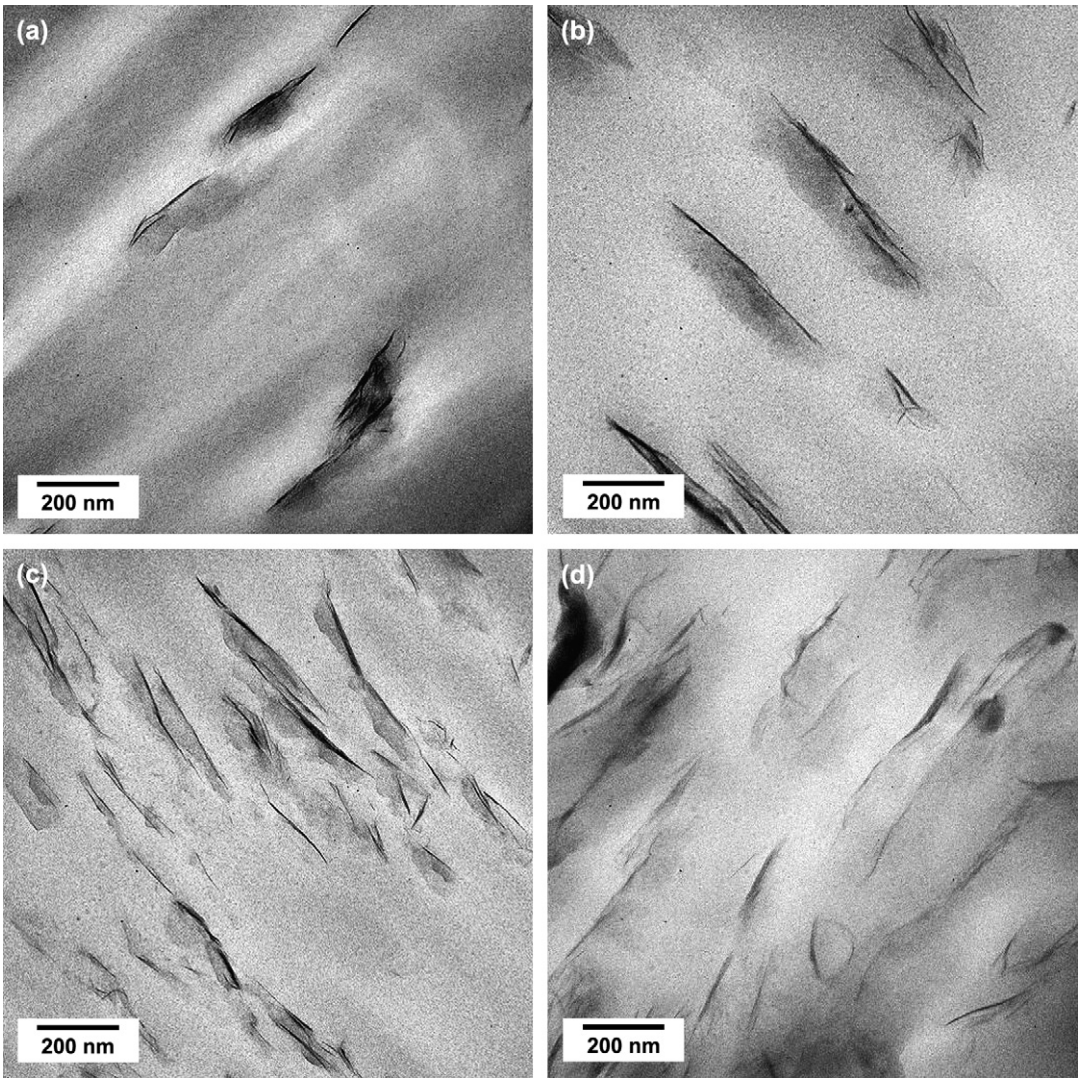

Fig. 1. TEM micrographs of PP composites with 1 wt% (a), 3 wt% (b), 5 wt% (c) and 7 wt% (d) of MMT at the ratio of PP-*g*-MA/organoclay of 1.0, viewed parallel to the transverse direction (TD).

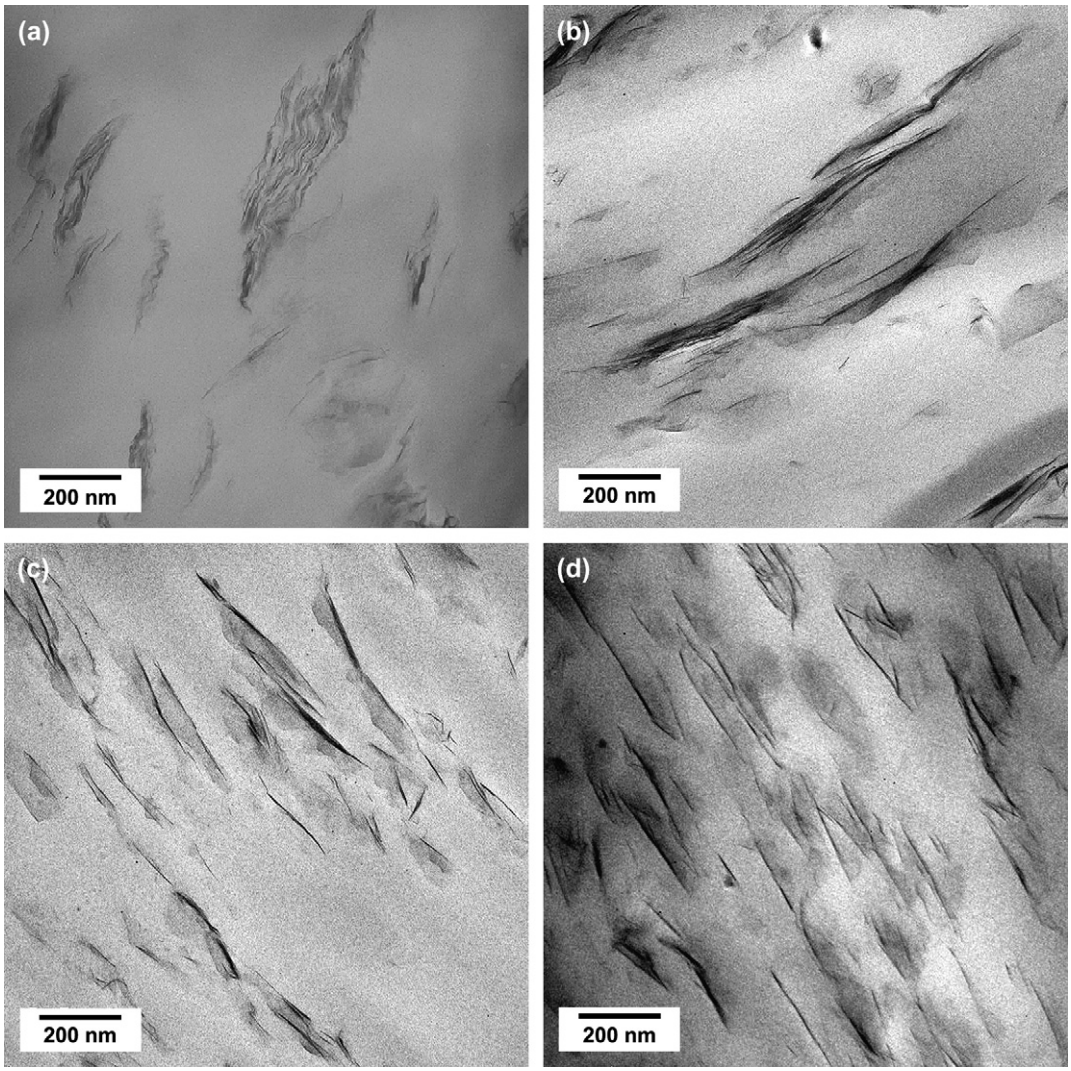

Fig. 2. TEM micrographs of PP composites at the PP-*g*-MA/organoclay ratio of 0 (a), 0.5 (b), 1.0 (c) and 2.0 (d) at a fixed MMT content of 5 wt%, viewed parallel to the transverse direction (TD).

of dispersion with a PP-*g*-MA/organoclay ratio of 2.0 seem much more significant than at a ratio of 0.5. The clay particles seem to be skewed and/or tilted at low PP-*g*-MA concentrations but show better alignment at higher concentrations. The length and thickness of the clay particles vary with MMT concentration in the nanocomposites at fixed ratios of PP-*g*-MA to organoclay. To quantify these issues, statistical analyses of the particle dimensions taken from these TEM images were performed.

TEM images, typically 30,000× in magnification for standard negative film, were electronically scanned and converted into grayscale tagged-image file format (TIFF) files. Quantitative image analysis was performed by opening a digital file in Adobe Photoshop where the dispersed platelets and/or agglomerates are traced over into an overlapped blank layer. To ensure accurate measurements of the particle length and thickness, the image is sufficiently magnified so that most of the particles, including single platelets, are counted. The resulting black/white layer file is imported into the image analysis program, SigmaScan Pro, which analyzes the traced particles, assigns each particle a numerical label, and exports the particle's length and thickness to separate files.

To ensure statistical validity of the analysis, 100–300 particles were counted to measure the length, thickness, and actual aspect ratio of particles for PP/PP-*g*-MA nanocomposites containing 1, 3, 5 and 7 wt% MMT at the ratio PP-*g*-MA to organoclay of 0, 0.5, 1.0 and 2.0. The results are summarized in Table 1. The experimentally determined MMT content of each nanocomposite after incineration is also shown in Table 1. Fig. 3 shows histogram of MMT particle length, thickness and pertinent statistical data obtained on PP/PP-*g*-MA/MMT nanocomposites containing 5 wt% MMT at a fixed PP-*g*-MA/organoclay ratio of 1.0. The sections were taken from the core region of injection molded specimens and viewed parallel to the TD so that the measurements were performed on particles presented in the FD–ND plane. The aspect ratios in this study were obtained by measuring the aspect ratio of each particle, which is a somewhat different

Table 1
Results of particle analysis for PP/PP-*g*-MA/MMT nanocomposites

MMT (wt%)	Total number of particles	Number average particle length (nm)	Weight average particle length (nm)	Number average particle thickness (nm)	Weight average particle thickness (nm)	Number average aspect ratio $\langle \ell/t \rangle_n$	Weight average aspect ratio $\langle \ell/t \rangle_w$	Aspect ratio[a] $\bar{\ell}_n/\bar{t}_n$	Aspect ratio[b] $\bar{\ell}_w/\bar{t}_w$
(a) PP-*g*-MA/organoclay = 0									
0.91	48	739	925	110	156	8	9	7	6
3.08	50	696	943	104	160	8	10	7	6
5.03	50	634	860	101	143	7	10	6	6
7.19	85	741	1010	95	152	10	15	8	7
(b) PP-*g*-MA/organoclay = 0.5									
0.93	163	241	341	10.0	13.7	28	42	24	25
2.99	219	219	319	10.6	18.5	25	38	21	17
5.15	232	233	317	11.3	16.1	25	38	21	20
7.22	289	225	287	11.3	18.5	24	30	20	16
(c) PP-*g*-MA/organoclay = 1.0									
0.97	150	238	268	4.8	6.1	56	67	49	44
3.00	229	217	304	5.7	9.5	45	54	38	32
5.38	225	173	206	4.9	7.8	44	56	35	26
7.36	241	175	215	5.0	10.3	43	53	35	21
(d) PP-*g*-MA/organoclay = 2.0									
0.91	120	187	225	4.7	5.8	48	67	40	39
2.92	194	170	217	4.4	5.8	42	52	38	37
5.16	270	181	224	3.8	4.4	51	63	48	51
7.27	280	193	232	4.2	5.1	48	55	45	45

[a] The values of the aspect ratio were computed from the number average particle length, $\bar{\ell}_n$, and thickness $\bar{t}_n$.
[b] The values of the aspect ratio were computed from the weight average particle length, $\bar{\ell}_w$, and thickness $\bar{t}_w$.

method than used in previous studies where the aspect ratio was calculated by dividing the average particle length by the average particle thickness [27,30–32].

The histograms show broad distributions in particle length and thickness as well as aspect ratio. Lee et al. showed the particle length to decrease with increasing MMT content while the particle thickness increased for PP nanocomposites made from a masterbatch whose ratio of PP-*g*-MA/organoclay was 1.0 [30]. Nam et al. reported similar trends in particle length and thickness with varying MMT content for PP-*g*-MA/clay nanocomposites [14]. As a result, the aspect ratio calculated by dividing the average particle length by the average particle thickness decreases as MMT content increases. On the other hand, this study shows how the particle dimensions depend on the ratio of PP-*g*-MA to organoclay. As shown in Fig. 4, both the particle length and the particle thickness decrease as more PP-*g*-MA is included in the formulation. The decrease is quite rapid at low PP-*g*-MA contents; but the particle dimensions change rather little as the PP-*g*-MA/organoclay ratio goes from 1 to 2. While particle length decreases with addition of PP-*g*-MA, the particle thickness decreases more rapidly (see Fig. 5). The net effect is an increase in aspect ratio shown in Fig. 6(a). Higher aspect ratios lead to increased reinforcement. However, for a fixed PP-*g*-MA/organoclay ratio, the aspect ratio decreases as the amount of MMT increases, see Fig. 6(b).

We note that the aspect ratio calculated by averaging the values for individual particles is generally larger than those calculated from the ratio of average particle length and the average particle thickness. Averaging the aspect ratios of individual particles leads to a weight average aspect ratio that is higher than the number average aspect ratio, as would be expected; however, aspect ratios calculated from the number average length and thickness are larger than that calculated from the corresponding weight average dimensions. We believe the current approach which has been made possible by improved image analysis techniques is more appropriate for modeling composite behavior as will be discussed later.

The WAXS scans taken from the skin portion of the injection molded specimen reveal that a strong peak from the organoclay persists in these nanocomposites without any significant shift in location; however, the intensity of this peak increases with increasing MMT content, indicating that large stacks of platelets exist in the skin portion of injection molded specimens. As pointed out by Lee et al., the situation may be rather different in the core of the specimen owing to the differences in the dispersion and orientation states of clay particles between the skin and core [30]. Interestingly, the peak for PP/organoclay composites without PP-*g*-MA appears to be shifted to a slightly higher angle; this could mean a collapse of the interlayer. The X-ray peak characteristic of the organoclay seems to be shifted very slightly to higher angles in some cases and to lower angles in others. These differences are so small that it is risky to attach any physical meaning to these very slight shifts. The WAXS results say very little about the morphology except that exfoliation is not complete, even then this technique can lead to false and incomplete interpretations of the nanocomposites. Direct observation by TEM is needed to get a better understanding of the state of dispersion

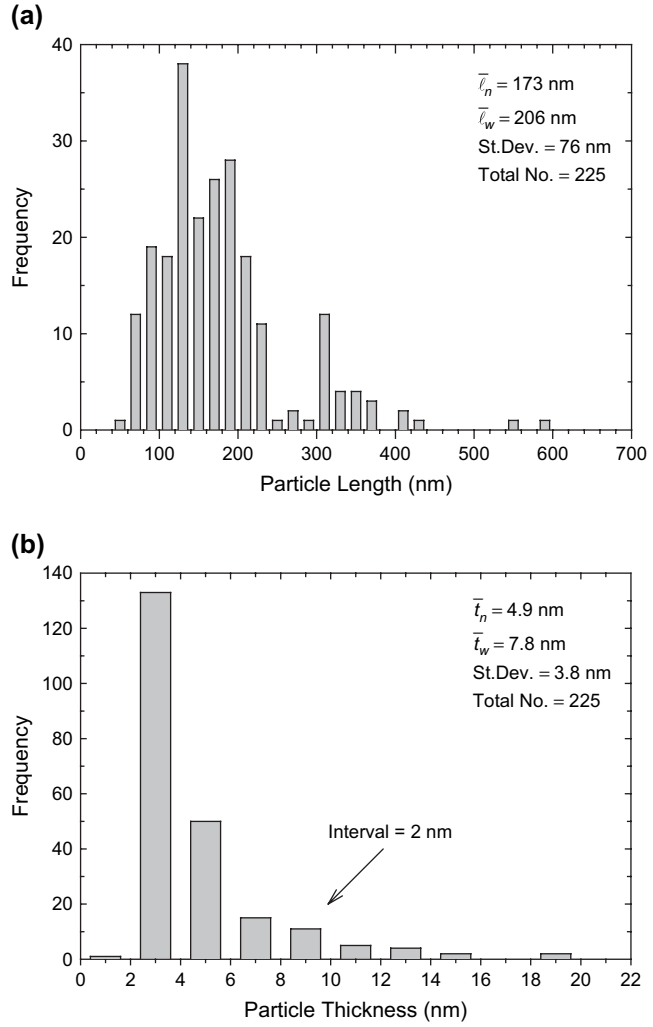

Fig. 3. Histogram of MMT particle lengths (a) and thickness (b) of PP/PP-*g*-MA/MMT nanocomposites at a fixed PP-*g*-MA/organoclay ratio of 1.0, viewed parallel to TD (MMT content = 5 wt%).

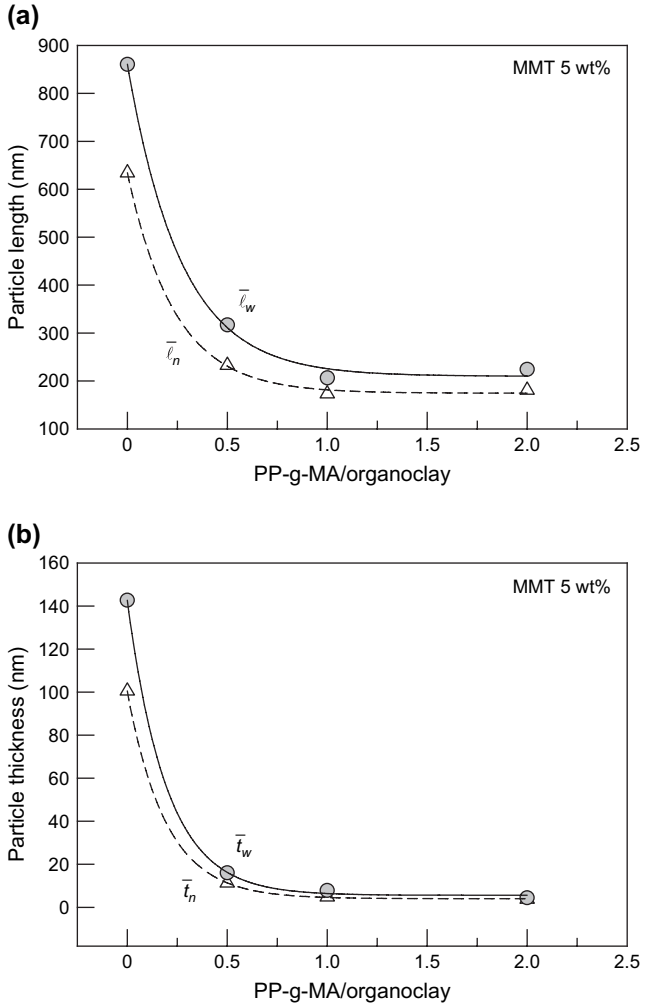

Fig. 4. The effect of PP-*g*-MA levels on particle length (a) and thickness (b) of PP/PP-*g*-MA/MMT nanocomposites at a fixed MMT content of 5.0 wt%.

[24,31,33]. However, the main problem with TEM is that the volume probed is very small and may not be representative of the nanocomposite as a whole. Therefore, bulk properties such as rheological/mechanical properties should be analyzed in addition to using both TEM and WAXS observations.

3.2. Performance of PP-based nanocomposites

3.2.1. Rheological properties

The melt rheological properties of nanocomposites provide fundamental insights about the processability and morphology for these materials. Viscoelastic measurements are highly sensitive to the nanoscale and mesoscale structure of the nanocomposites and appear to be a powerful method to probe the state of dispersion in such materials [15,20,34–36]. The addition of organoclay to polymer matrix increases the storage modulus by several orders of magnitude and alter the shear-thinning behavior at low frequencies to indicate a transition from liquid-like ($G' \propto w^2$, $G'' \propto w^1$) to solid-like (G', $G'' \propto w^0$) rheological behavior. It is generally believed that the extent of these changes reflects the state of dispersion of the clay. This has been attributed to the formation, in the quiescent state, of a percolated network superstructure of the

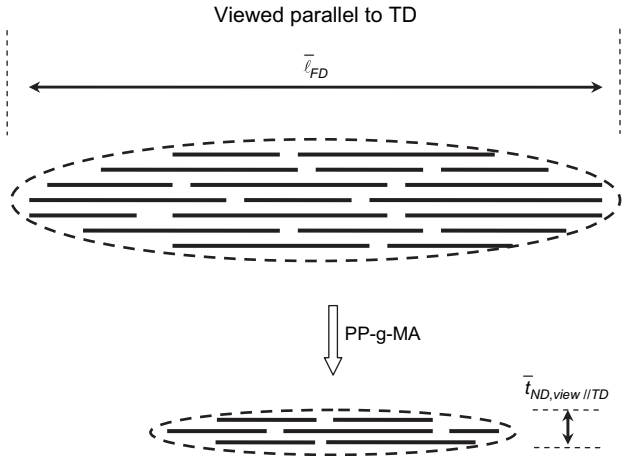

Fig. 5. Schematic illustration of the change of effective organoclay particle length and thickness when viewed along the FD in PP nanocomposites as PP-*g*-MA is added.

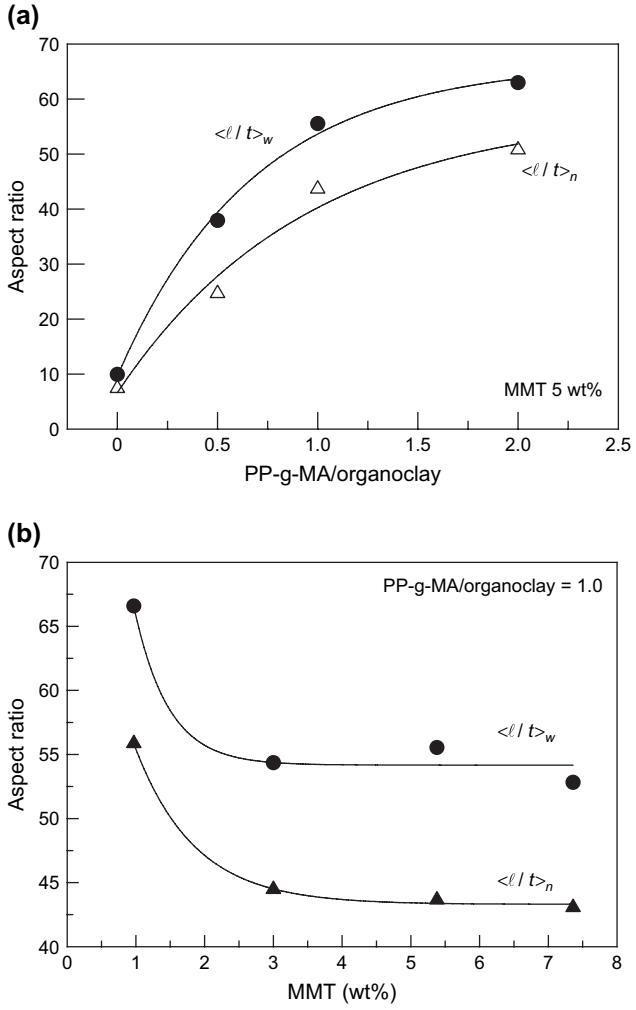

Fig. 6. The effect of MMT content (a) and PP-*g*-MA levels (b) on number and weight average aspect ratio of PP/PP-*g*-MA/MMT nanocomposites.

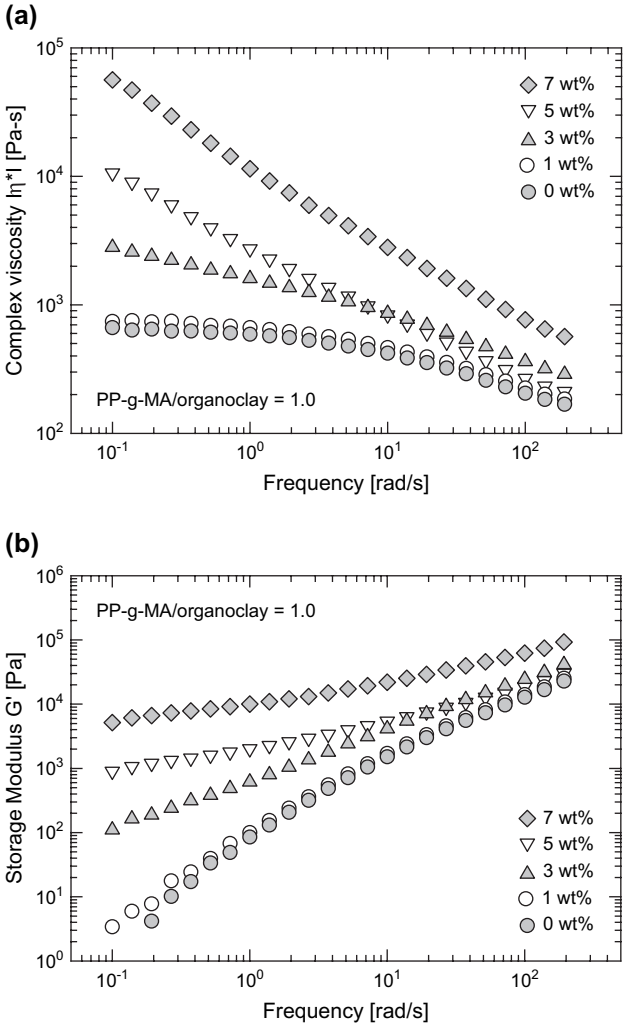

Fig. 7. Frequency sweep results for PP nanocomposites at 180 °C: complex viscosity (a) and storage modulus (b) at a fixed ratio PP-*g*-MA to organoclay of 1.0.

exfoliated layers or stacks of intercalated layers called tactoids [15,35,36]. The significant lowering of the percolation threshold as compared to the case of isotropic spheres is due to the anisotropy of the tactoids or individual platelets that prevent a free rotation of these elements and dissipation of stress. The extent of percolation of the network can increase in two ways: one is to increase the number of stacks based on the assumption that layer thickness and size are the same (Case I). The other is to increase the degree of exfoliation (Case II). Case I would correspond to increasing of the amount of clay at fixed PP-*g*-MA content while Case II would correspond to increasing the PP-*g*-MA content at fixed clay content.

Based on these points of view, frequency sweeps for PP nanocomposites were made with different amounts of clay and PP-*g*-MA at 180 °C. Fig. 7 shows the rheological properties for PP nanocomposites with different clay amounts at a fixed PP-*g*-MA/organoclay ratio of 1.0. Compared with pure PP, the moduli increase progressively and their slopes become more negative at low frequencies as clay content increases. The complex viscosity also shows an increased shear-thinning behavior. As mentioned above, this is attributed to the percolated network by the increase in the content of clay particles (Case I). Fig. 8 shows the rheological properties for PP nanocomposites with various PP-*g*-MA/organoclay ratios at fixed MMT of 5 wt%. Compared with pure PP, the moduli also increase progressively and the slopes become progressively more negative at low frequencies as the PP-*g*-MA content increases. As mentioned above, this is attributed to the percolated network by an increase of degree of exfoliation due to the increase of the amount of compatibilizer (Case II). These trends are consistent with the TEM observations in the previous section.

3.2.2. Mechanical properties and reinforcement effect

Fig. 9(a) shows the effect of MMT content on the tensile modulus of PP nanocomposites for various PP-*g*-MA/organoclay ratios. The addition of MMT to PP results in a significant increase in stiffness at low MMT concentrations, i.e., <2–3%, while the rate of increase beyond this loading is less pronounced. Similar trends are evident for PP/PP-*g*-MA/MMT nanocomposites, but the extent of reinforcement is

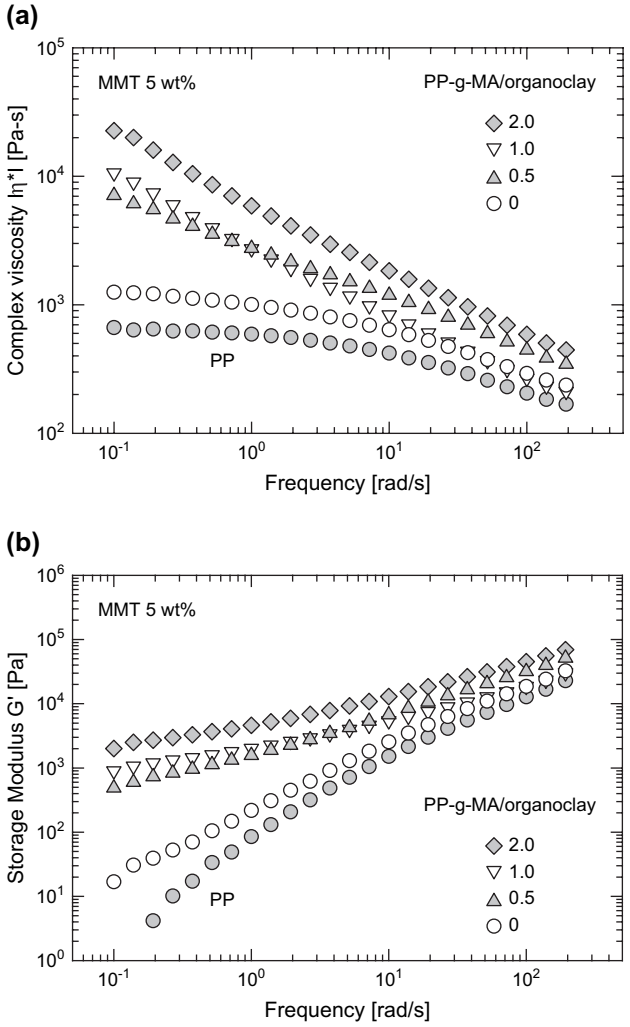

Fig. 8. Frequency sweep results for PP nanocomposites at 180 °C: complex viscosity (a) and storage modulus (b) with different ratios of PP-*g*-MA/organoclay at a fixed MMT content of 5 wt%.

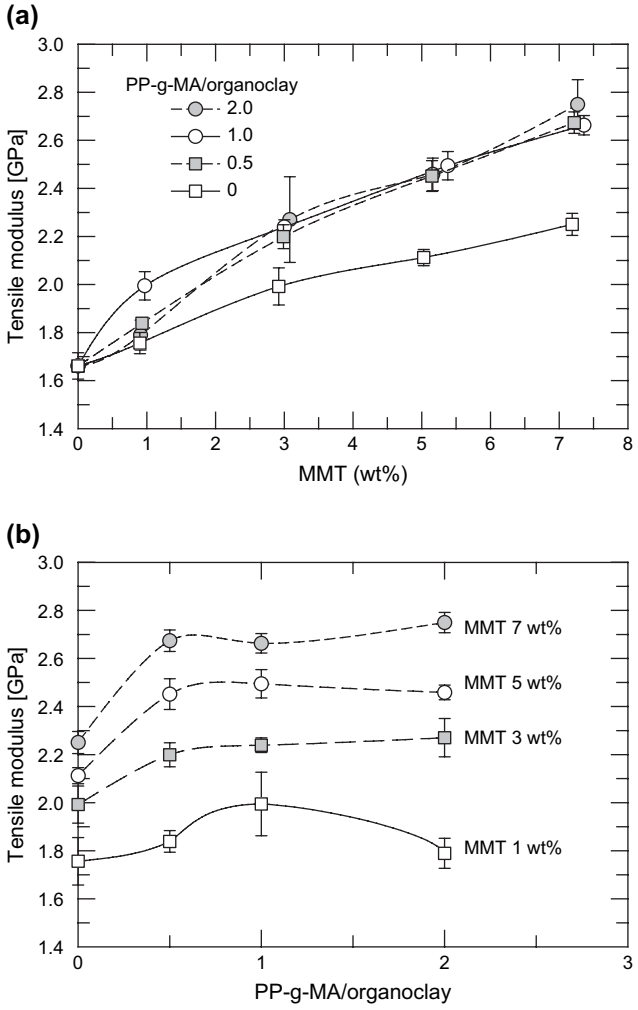

Fig. 9. Effect of MMT content on the tensile modulus for various PP-*g*-MA/organoclay ratios (a). Tensile modulus versus ratio of PP-*g*-MA to organoclay for different MMT levels (b).

significantly higher. Interestingly, the increase in tensile modulus caused by the PP-*g*-MA seems to be rather independent of the amount of PP-*g*-MA added. This point is made clear in Fig. 9(b) where the tensile moduli are plotted versus the PP-*g*-MA/organoclay ratio at fixed MMT contents. As reported in the prior literature, PP-*g*-MA is needed to achieve better dispersion of the silicate platelets in a PP matrix and, as a consequence, improved stiffness of PP nanocomposites. As mentioned above, the degree of exfoliation, distribution and orientation of clay platelets in the direction of flow in PP nanocomposites and the rheological properties of nanocomposites containing PP-*g*-MA in a 2:1 ratio with organoclay are much enhanced compared to compositions based on a ratio of 0.5. However, the tensile modulus seems relatively insensitive to the PP-*g*-MA/organoclay ratio in this range.

We speculated that the origin of this apparent contradiction might result from a lowering of the modulus of the matrix as PP-*g*-MA is added to PP. To confirm this, we examined the effect of PP-*g*-MA content on the matrix properties. Fig. 10 shows the tensile modulus of PP/PP-*g*-MA mixture without MMT. Clearly, the modulus decreases as the amount of PP-*g*-MA increases. This is due to the lower crystallinity of PP-*g*-MA than that of PP. This issue will be addressed in more detail in a subsequent paper. The upper line in Fig. 10(b) shows the observed reinforcement effect as the MMT content is increased for a fixed ratio of PP-*g*-MA/organoclay of 2.0. The lower line in Fig. 10(b) shows the modulus of the PP/PP-*g*-MA mixture in these nanocomposites at each MMT level using the data in Fig. 10(a) and the fact that the ratio of PP-*g*-MA to organoclay is 2.0 and the mass of organoclay/mass of MMT = 1.67 in this study. The ratio of the nanocomposite modulus to that of the polymer matrix provides a useful way to judge the extent of reinforcement. Fig. 11 shows such ratios as a function of MMT content and as a function of PP-*g*-MA/organoclay ratio. The lower curves in each case show the "apparent" reinforcement obtained by regarding PP as the matrix while the upper lines show the "true" reinforcement effect by using the measured modulus of the PP/PP-*g*-MA mixture in each composition. Higher content of PP-*g*-MA leads to better exfoliation and a corresponding increase in reinforcement; however, in

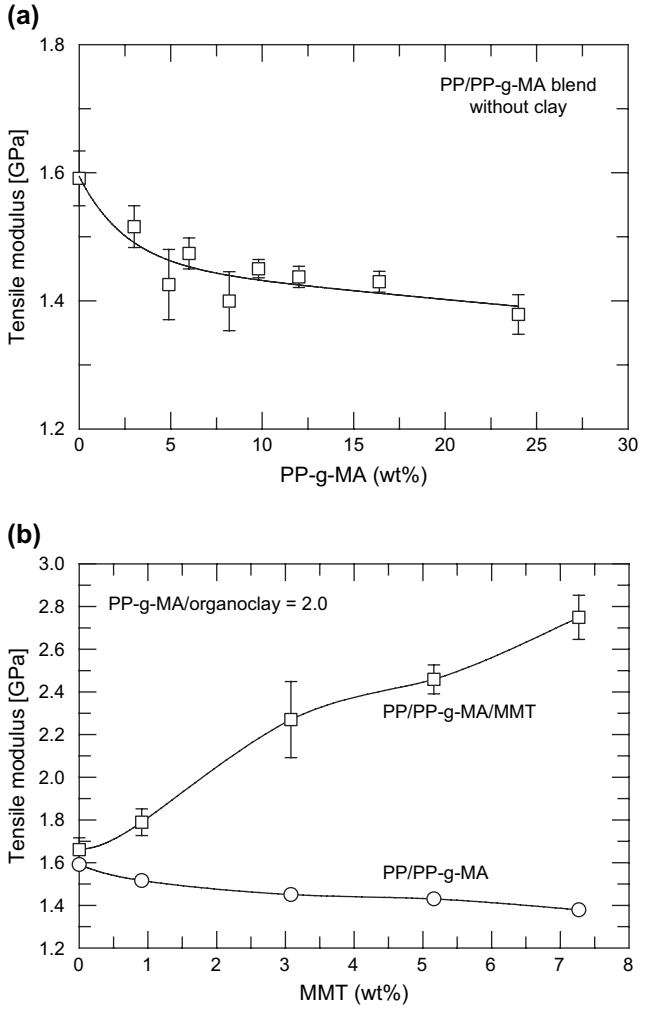

Fig. 10. Tensile modulus for PP/PP-*g*-MA mixture without clay (a) and for a nanocomposite versus wt% MMT where the PP-*g*-MA/organoclay ratio of 2 (upper curve) and for the mixture of PP/PP-*g*-MA that forms the matrix at each MMT level (lower curve) (b).

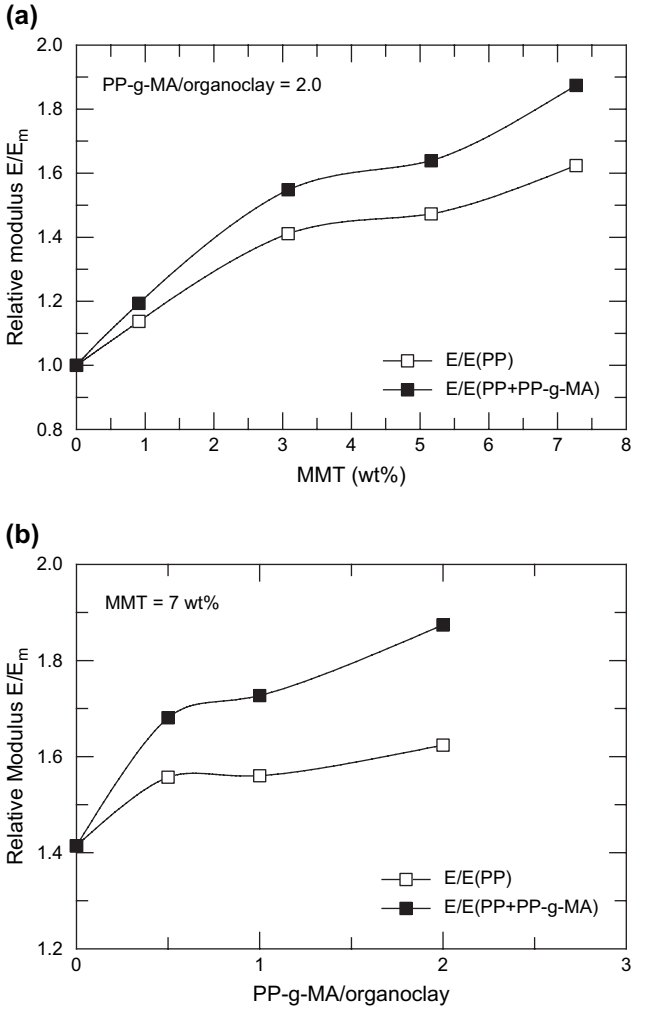

Fig. 11. The relative modulus versus MMT wt% (a) and PP-*g*-MA/organoclay ratio (b) where the data are normalized by the modulus of PP and by that of the appropriate PP/PP-*g*-MA mixture.

a practical sense, the full benefit is compromised by the lower modulus of PP-*g*-MA. Clearly, it would be useful to be able to maleate PP without reducing its crystallinity.

The elongation at yield and at break for PP/PP-*g*-MA/MMT nanocomposites at various ratios of PP-*g*-MA to organoclay are shown in Fig. 12. The elongation at yield generally decreases as MMT content increases irrespective of PP-*g*-MA/organoclay ratio. The elongation at break for homopolymer PP is above 200% and decreases to 60–80% at an MMT content of 1 wt%. The elongation at break data show a relatively large standard deviation as indicated by the error bars in Fig. 12. However, it is clear that the addition of MMT leads to a significant decrease in elongation at break. The dependence of yield strength on MMT content and PP-*g*-MA content of these PP nanocomposites is shown in Fig. 13. Composites without PP-*g*-MA elongated beyond the yield point before fracturing for all MMT loadings up to 7 wt%. The yield strength increases at low MMT content (1 wt%) and generally decreases upon adding additional MMT. The elongation at yield also decreases with the amount of MMT and the composites failed in a brittle manner at higher MMT contents. Interestingly, the elongation at the onset of brittle fracture decreases as the PP-*g*-MA content increases. It is clear that the addition of MMT leads to a significant decrease in elongation at break, as expected, and increased amounts of PP-*g*-MA accelerate the decrease in elongation at break. Fig. 13(b) shows how the relative yield strength varies with the ratio of PP-*g*-MA/organoclay at fixed clay content. The relative yield strength is defined as the yield strength of PP nanocomposites over that of PP. As the ratio increases, relative yield strength shows a maximum and then decreases slowly. The maximum value increases as more PP-*g*-MA is added. Generally, the yield strength reflects, among other factors, the nature of the interface between polymer and filler. As more PP-*g*-MA is added, better exfoliation is achieved as mentioned above. It is also believed that this increases the interfacial adhesion between polymer and the exfoliated MMT layers, resulting in an increase of the yield strength.

Fig. 14 shows the influence of both the PP-*g*-MA and MMT contents on notched Izod impact strength. These are averages of values from the far end and the gate end samples because

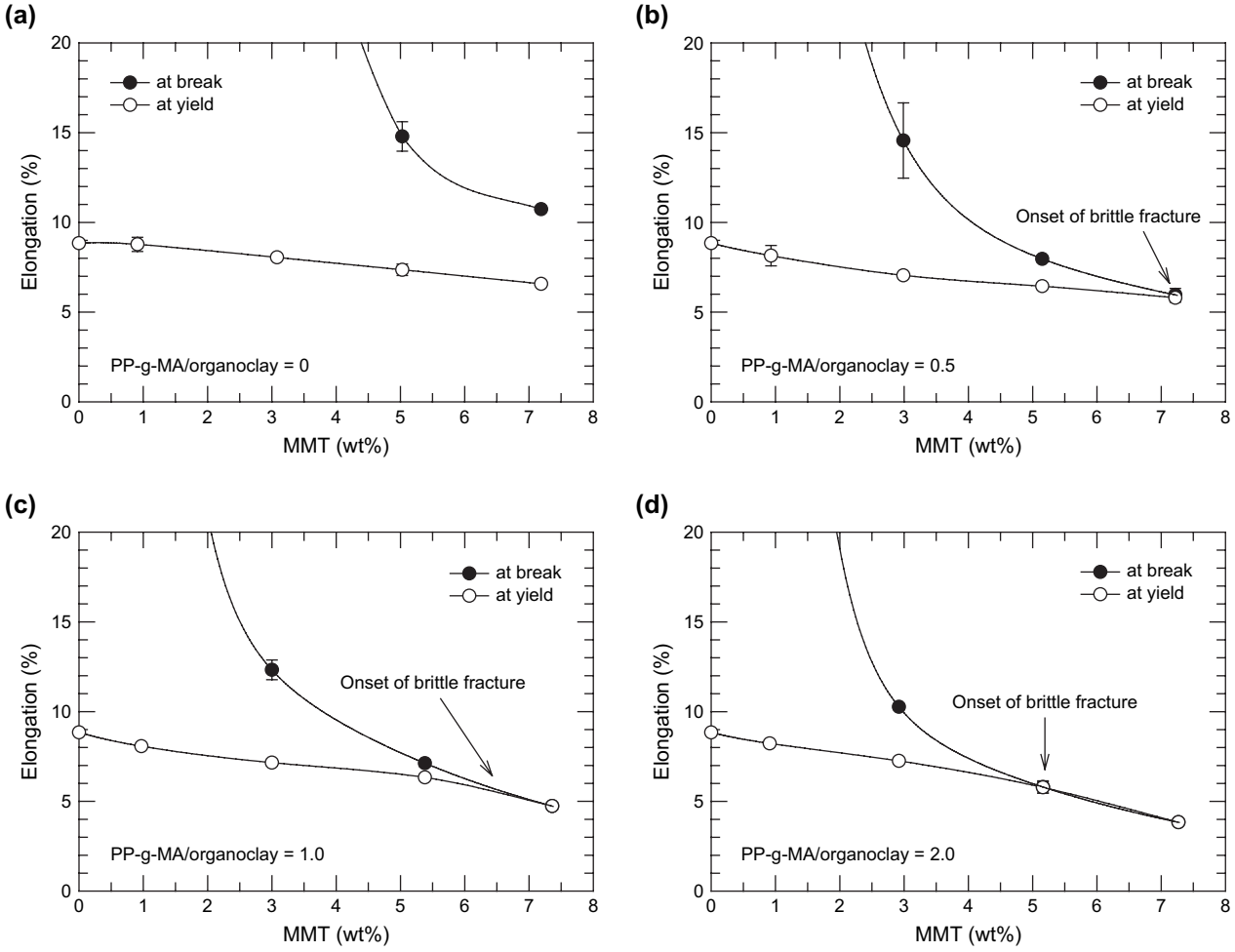

Fig. 12. Elongation at break and at yield versus MMT wt% for different ratios of PP-*g*-MA to organoclay: (a) 0, (b) 0.5, (c) 1.0 and (d) 2.0.

the difference between the two is relatively small. Generally, reinforcement reduces the Izod impact strength and as expected, the addition of MMT makes the materials more brittle; however, PP itself is very brittle by this test, thus, it is not surprising, that all these materials exhibit complete breakage of specimens during the impact tests, irrespective of the amount of PP-*g*-MA and MMT.

3.2.3. Thermal expansion behavior

PP and PP-based nanocomposites show significant nonlinearity in thermal expansion as the temperature increases as reported by Lee et al. [37]. Thus, all data presented in this paper were obtained over 0–30 °C temperature range during a second heating scan of these nanocomposites since such values should be related to the mechanical property data measured at room temperature, i.e., ca. 25 °C. Fig. 15(a) shows the coefficients of linear thermal expansion (CTEs) obtained from the second heating in the flow direction for the PP/PP-*g*-MA/MMT nanocomposites as a function of the MMT content. While the CTE decreases slightly for PP/MMT composites without any PP-*g*-MA on addition of MMT, the CTEs for PP nanocomposites containing PP-*g*-MA decrease much more as the MMT content is increased. This reflects the increased degree of exfoliation and better orientation of the clay platelets in the flow direction when PP-*g*-MA is added. However, replotting the data versus the ratio of PP-*g*-MA to organoclay as shown in Fig. 15(b), it is clear that the CTE does not decrease significantly as higher amounts of PP-*g*-MA are included at a fixed MMT content. These unexpected results are consistent with the modulus data and should be analyzed by considering the change in the matrix properties caused by adding PP-*g*-MA.

For better understanding of the thermal expansion behavior of these nanocomposites, the CTE of the nanocomposites is normalized by the corresponding PP or PP/PP-*g*-MA blend without MMT. Since PP-*g*-MA has a higher thermal expansion coefficient than PP, the CTE of a PP/PP-*g*-MA blend without MMT increases as the amount of PP-*g*-MA increases as shown in Fig. 16(a). The solid lines in Fig. 16(b) show the nanocomposite CTE data normalized by the CTE of the PP/PP-*g*-MA matrix while the dashed lines correspond to normalization by the CTE of PP. At the lower PP-*g*-MA/organoclay ratio of 0.5, the method of normalization does not matter; however, normalization by the CTE of the PP/PP-*g*-MA matrix leads to slightly lower values at the higher PP-*g*-MA/organoclay ratios. We note that adding PP-*g*-MA lowers the modulus which

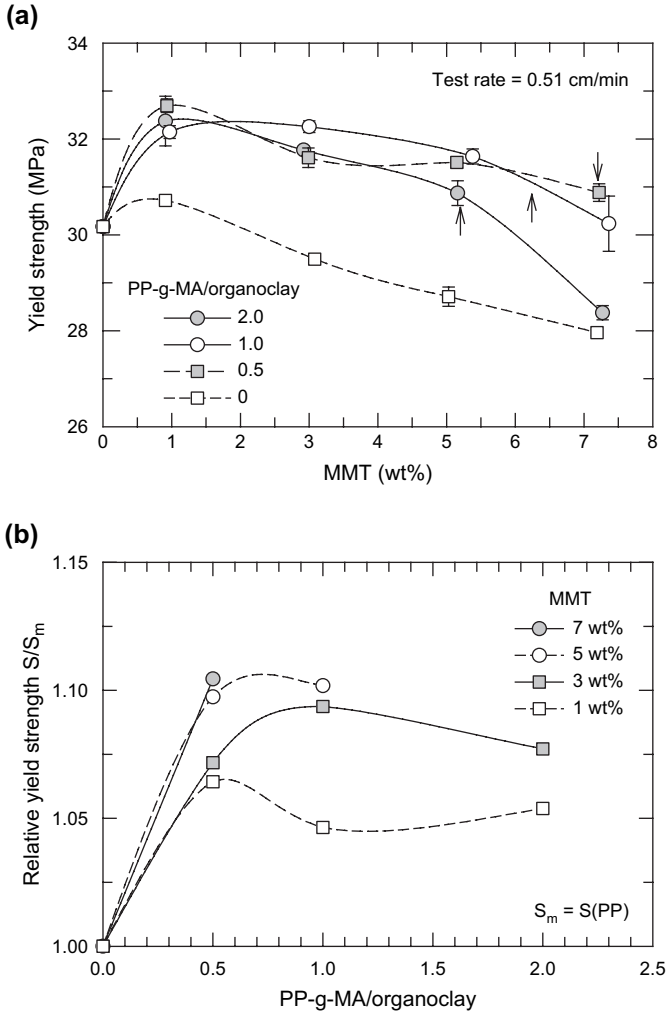

Fig. 13. Yield strength as a function of MMT content for different ratios of PP-*g*-MA to organoclay.

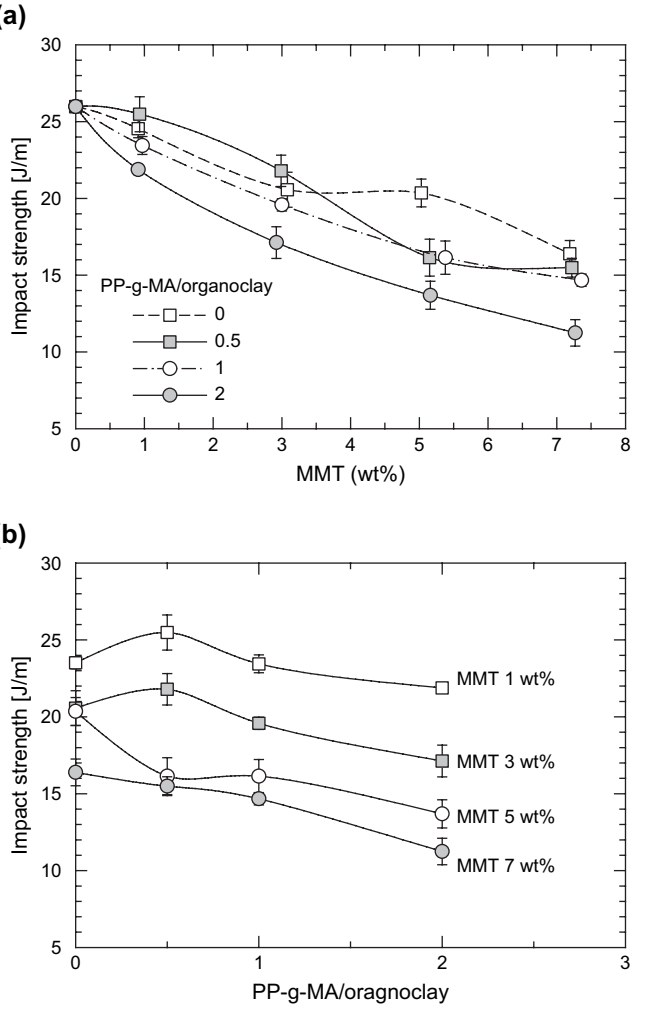

Fig. 14. Effect of PP-*g*-MA content on notched impact strength of nanocomposites as a function of the montmorillonite content (a) and the ratio of PP-*g*-MA to organoclay (b).

makes it easier for the filler to restrain the expansion of the composite; however, the main effect of the PP-*g*-MA is to increase the filler aspect ratio. In a practical sense, the full benefit of the latter is compromised by the higher expansion of PP-*g*-MA which is similar to the effect on nanocomposite modulus. Therefore, the amount of PP-*g*-MA added along with its crystallinity play important roles in optimizing mechanical and thermal expansion properties.

3.3. Modeling

The effects of filler characteristics, e.g., modulus, aspect ratio, orientation, shape, volume fraction, etc., on the properties of composites have been extensively discussed in the literature. Among those characteristics, the aspect ratio of the filler is a particularly important factor for nanocomposites since high aspect ratios can contribute to greater increase in modulus and greater reduction in thermal expansion. There have been some reports on the modeling for nanocomposites based on nylon 6 using the Halpin–Tsai, Mori–Tanaka and Chow theories [27,28,38]. Sheng et al. have recently reported a multiscale micromechanical modeling of amorphous and semi-crystalline polymers, e.g., nylon 6–clay nanocomposites based on the effective clay particle by comparing numerical and analytical models [39]. Among the models, the Chow model appears to be the only option for predicting the linear thermal expansion of composites containing anisotropic particles of finite aspect ratios. This model is relatively simple to use and has the advantage of predicting the elastic modulus on the same physical basis. Using the two models developed by Chow may enable us to correlate the thermal expansion behavior with the mechanical properties of composites, i.e., tensile modulus.

In the Chow models, the filler is considered to be aligned ellipsoidal particles and the anisotropic effect is characterized by the ratio of the major to minor axes, $\rho = c/a$ [40,41]. For a composite consisting of perfectly aligned ellipsoidal particles embedded in a matrix, the longitudinal Young's modulus, E, is given by:

$$\frac{E - E_m}{E_m \phi} = \frac{\left(k_f/k_m - 1\right)G_3 + \left(\mu_f/\mu_m - 1\right)\left(G_3\xi + K_3\zeta\right)}{2K_1G_3 + G_1K_3} \quad (1)$$

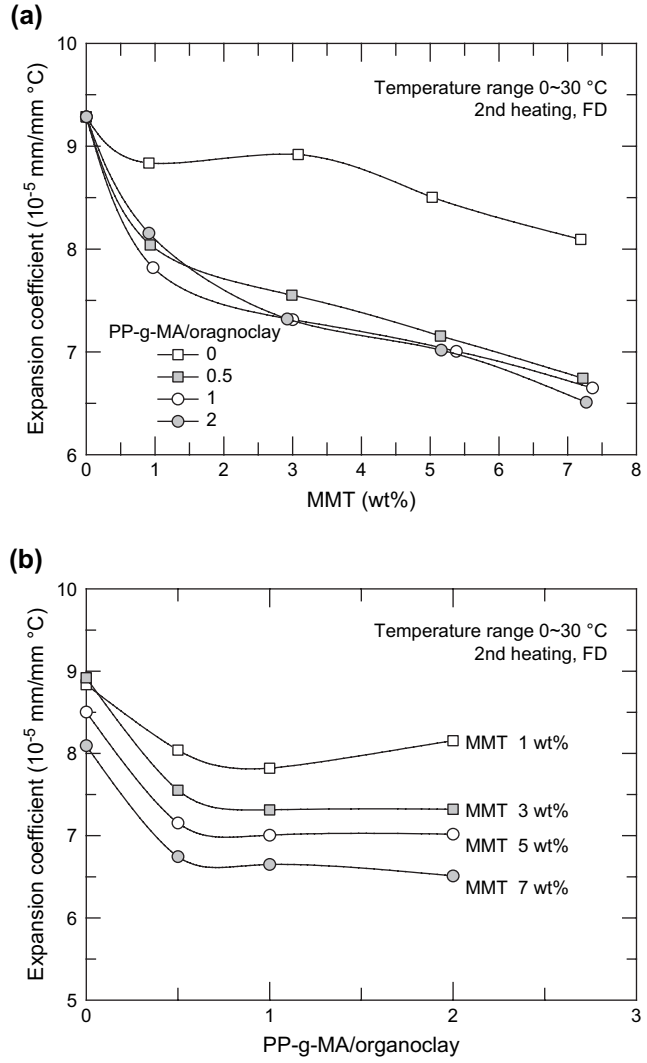

Fig. 15. Effect of PP-*g*-MA content on the linear thermal expansion coefficient of nanocomposites as a function of the montmorillonite content (a) and the ratio of PP-*g*-MA to organoclay (b).

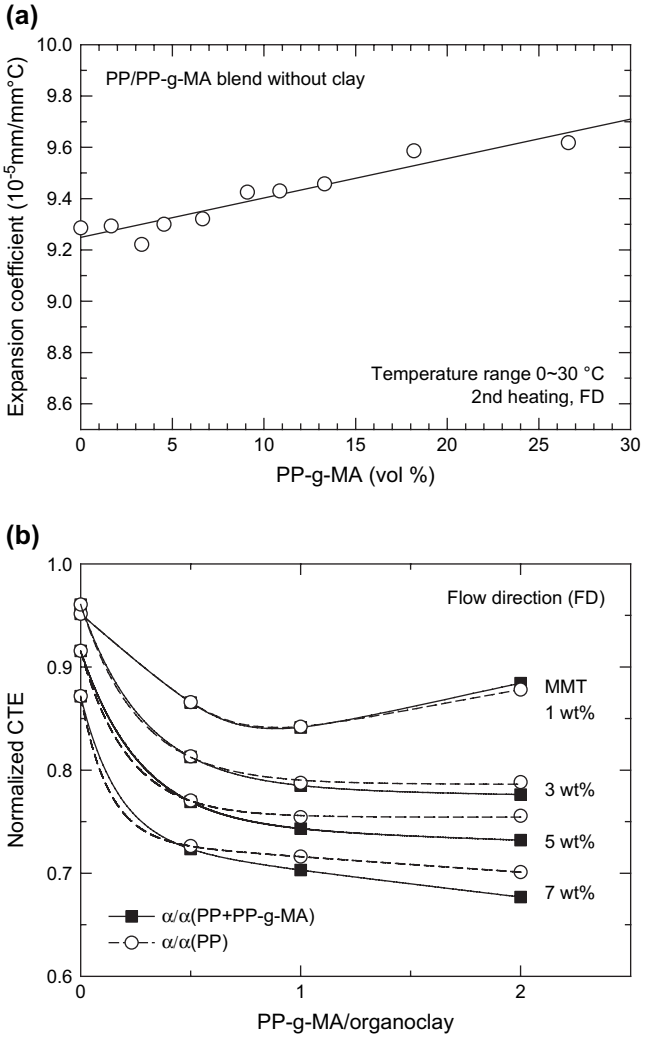

Fig. 16. Thermal expansion coefficient for PP/PP-*g*-MA mixture without clay (a) and the relative thermal expansion coefficient versus PP-*g*-MA/organoclay ratio (b) where the data are normalized by the coefficient of PP and by that of the appropriate PP/PP-*g*-MA mixture.

where ϕ is the volume fraction of particles and ξ and ζ are defined as follows:

$$\xi = \frac{K_1}{1 + 2(\mu_f/\mu_m - 1)(1-\phi)S_{1212}} \tag{2}$$

$$\zeta = \frac{1 + (\mu_f/\mu_m - 1)(1-\phi)(S_{1111} - S_{3311})}{1 + 2(\mu_f/\mu_m - 1)(1-\phi)S_{1212}} \tag{3}$$

where k_f and k_m refer to the bulk modulus while μ_f and μ_m are the shear modulus for the filler and matrix, respectively. Here Eshelby's tensor S is a function of the aspect ratios of an ellipsoidal particle. The bulk and shear moduli, k and μ, are used to calculate K_i and G_i functions [40]:

$$K_i = 1 + \left(\frac{k_f}{k_m} - 1\right)(1-\phi)\alpha_i \tag{4}$$

$$G_i = 1 + \left(\frac{\mu_f}{\mu_m} - 1\right)(1-\phi)\beta_i \tag{5}$$

where α and β are functions of ρ and Poisson's ratio of the matrix.

The longitudinal thermal expansion coefficient, i.e., in the direction parallel to the major axis of the particle, is given by:

$$\alpha_L = \alpha_m + \frac{k_f}{k_m}\frac{(\gamma_f - \gamma_m)G_1\phi}{2K_1G_3 + G_1K_3} \tag{6}$$

while the transverse thermal expansion coefficient, in the normal direction to the major axis of the particle is given by:

$$\alpha_T = \alpha_m + \frac{k_f}{k_m}\frac{(\gamma_f - \gamma_m)G_3\phi}{2K_1G_3 + G_1K_3} \tag{7}$$

where γ_f and γ_m are bulk thermal expansion coefficient for the filler and matrix, respectively. K_i and G_i are functions of k and μ [28,41].

A key issue in the modeling for polymer nanocomposite lies in how to define the dispersion state of the clay layers. Generally modeling is carried out based on the assumption of fully exfoliated and well-oriented clay layers. However, in most cases, exfoliation is thermodynamically unfavorable and most synthesis processes lead to particles comprised of multiple platelets dispersed in the polymer matrix. To consider the influence of incomplete exfoliation on the nanocomposites, we assume that organoclay particles can be treated, as previously suggested by Fornes and Paul [38] and that tensile modulus of a particle in the direction parallel to the particle long axis and the individual MMT platelets (see Fig. 6) can be estimated by using the following rule of mixtures, as suggested by Brune and Bicerano [42]:

$$E_p = \upsilon_{MMT} E_{MMT} + \upsilon_{gallery} E_{gallery} \tag{8}$$

where υ_{MMT} and $\upsilon_{gallery}$ are the volume fractions of silicate layers in the stack and gallery space, respectively. $E_{gallery}$ is the modulus of the material in the gallery which is expected to be much less than E_{MMT}. The volume fraction of particles in the composites can be estimated simply as follows:

$$\phi_p = \frac{\text{volume of MMT}}{\text{volume of nanocomposite}} \times \frac{\text{volume of particle}}{\text{volume of MMT}} = \frac{\phi_{MMT}}{\upsilon_{MMT}} \tag{9}$$

The volume fraction of MMT in the dispersed particles of organoclay can be well approximated from the ratio of the d spacing of pure MMT ($d_{001} = 0.96$ nm) and the d spacing obtained from X-ray scans of the PP nanocomposites (2.42 nm as reported above) to give $\upsilon_{MMT} = 0.96/2.4 \approx 0.40$. Based on Eq. (8), the tensile modulus of these particles would be $E_p \approx \upsilon_{MMT} E_{MMT} = (0.40)(178\ \text{GPa}) = 70.6$ GPa where the tensile modulus of MMT is 178 GPa [43,44]. Note that the volume fraction of organoclay particles is higher than that of silicate platelets at the same weight percent of MMT.

In this approach, we consider the particles to consist of multiple organically modified clay platelets aligned parallel to the particle long axis (see Fig. 6). For these calculations, the following parameters are used: $E_p = 70.6$ GPa, $E_{PP} = 1.59$ GPa, Poisson's ratio of the matrix, $\nu_m = 0.38$ [45] and Poisson's ratio of the particle, $\nu_p = 0.26$ (or 0.32), $\gamma_f = 0.5 \times 10^{-5}\ ^\circ\text{C}^{-1}$ [46] and bulk thermal expansion coefficient of the matrix is calculated from experimental data for pure PP using $\gamma = \sum \alpha_i$. Bulk and shear moduli for isotropic materials are interrelated by $k = E/3(1-2\nu)$ and $\mu = E/2(1+\nu)$, respectively [47]. The normalized modulus and CTE calculated from the model consider the lower modulus and higher thermal expansion of the matrix caused by the presence of PP-*g*-MA. The values of the matrix modulus and CTE for PP/PP-*g*-MA blends without MMT as a function of organoclay particle volume fraction can be obtained from regression of data in Figs. 10(a) and 16(a), respectively. The Poisson's ratio of the particles can be estimated by the simple mixing rule, $\nu_p = \nu_{MMT}\upsilon_{MMT} + \nu_{gallery}\upsilon_{gallery}$, where $\nu_{MMT} = 0.20$ [47] and $\nu_{gallery} = 0.35$–0.50. We note that the calculations are not sensitive to the value of Poisson's ratio of the particle within the range 0.26–0.32.

Fig. 17 compares the experimental values of tensile modulus and CTE for PP nanocomposites for various PP-*g*-MA/organoclay ratios described earlier with the predictions of the Chow theory as a function of particle volume fraction for different values of particle aspect ratio. The particle aspect ratios obtained by matching the experimental data to the theoretical values predicted by the Chow model are summarized in Table 2. As seen in Fig. 17(a), the experimental modulus data do not fall along the curve of any single aspect ratio. The predicted aspect ratio obtained by comparing the experimental data with the theory decreases as MMT loading increases in nanocomposites. This suggests that the degree of exfoliation and/or particle orientation of the clay platelets tends to decrease with increasing MMT content. Fig. 17(b) compares the measured CTEs in the FD for PP nanocomposites with the theoretical predictions of the Chow model as a function of particle volume fraction and aspect ratio at

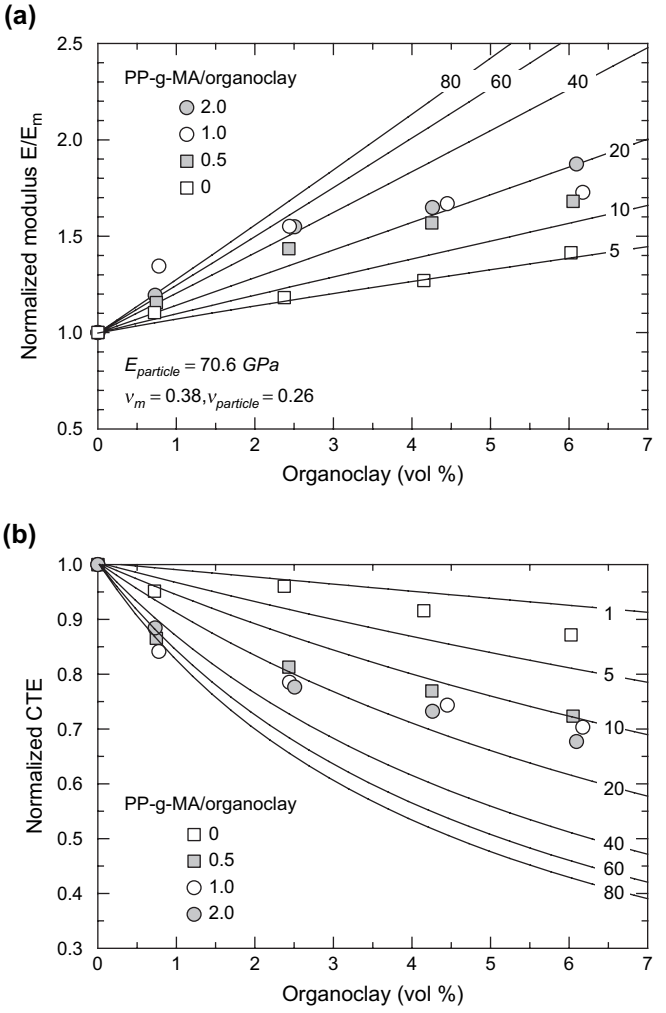

Fig. 17. Comparison of theoretical tensile modulus (a) and CTEs (b) for different aspect ratios in the flow directions predicted by the Chow model with experimental data for PP nanocomposites at different ratios of PP-*g*-MA to organoclay.

Table 2
Aspect ratio of clay particles obtained by comparing experimental mechanical and thermal data for PP/PP-*g*-MA/MMT nanocomposites at different ratios of PP-*g*-MA to organoclay to predicted values using the Chow model

MMT (wt%)		Aspect ratio of fillers predicted from Chow model using							
		Tensile modulus				Linear thermal expansion coefficient			
PP-*g*-MA/organoclay ratio		0	0.5	1.0	2.0	0	0.5	1.0	2.0
1	Model[a]	40	36	>160	40	15	60	100	60
	TEM[b]	8	28	56	48				
3	Model[a]	12	26	50	35	<5	16	24	24
	TEM[b]	8	25	45	42				
5	Model[a]	9	16	22	19	<5	11	14	15
	TEM[b]	7	25	44	51				
7	Model[a]	9	12	15	18	<5	9	12	12
	TEM[b]	10	24	43	48				

[a] E/E_m versus ϕ_p, $E_p = 70.6$ GPa, $\nu_m = 0.38$, $\nu_p = 0.2594$, where $E_m = E_{PP}$ + PP-*g*-MA.
[b] Number averaged aspect ratio, $\langle \ell/t \rangle_n$.

different PP-*g*-MA/organoclay ratios. Similar to the observations described above for modulus, CTEs in the FD do not match any single line for a fixed aspect ratio and the same general trend is observed, i.e., the predicted aspect ratio obtained by comparing experimental data with theory decreases as MMT content increases irrespective of PP-*g*-MA/organoclay ratio.

The trends in aspect ratio obtained by comparing the theory with the mechanical and thermal data are similar to those obtained by TEM; however, the absolute values are somewhat different. The aspect ratio for PP-*g*-MA/organoclay = 0.5 follows this order: thermal (60) > mechanical (36) > TEM (28) for 1 wt% MMT and TEM (24) > mechanical (12) > thermal (9) for 7 wt% MMT (Table 2). The aspect ratio for PP-*g*-MA/organoclay = 2.0 goes like this: thermal (60) > TEM (48) > mechanical (40) for 1 wt% MMT and TEM (48) > mechanical (18) > thermal (12) for 7 wt% MMT (Table 2). In this case, the model requires higher values of the aspect ratio at lower MMT content and generally lower values at higher MMT content to match the property measurement than those that were determined by morphological observations. When the particles are treated as single platelets (comprised of 100% MMT with a modulus of 178 GPa), the line predicted by the model requires much higher values of aspect ratio than those measured from TEM observations because the volume fraction of particles is underestimated. We note that the discrepancy between the morphological observation and the line predicted or the measured aspect ratio is believed to stem from incomplete orientation of the particles or the inadequacies of the model and the parameter estimations used.

To analyze this clearly, we carried out the modeling by considering several factors such as modulus, volume fraction and degree of exfoliation of the particles. Fig. 18 shows four simplified cases for the modeling selected to help us understand

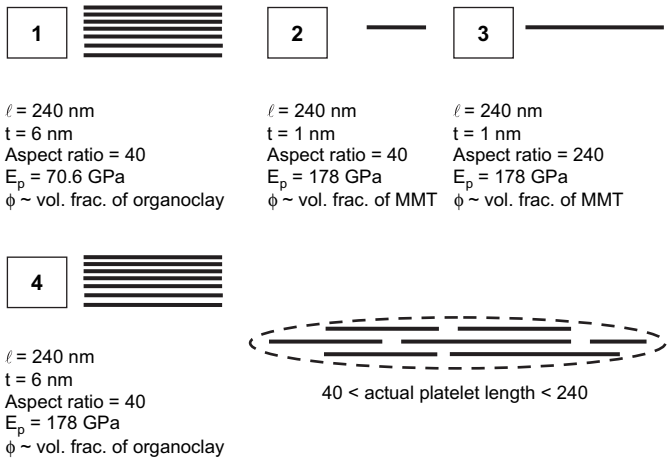

Fig. 18. Schematic diagrams of four cases to be modeled to show the effect of aspect ratio, tensile modulus and volume fraction of particles.

the relative importance of each factor. First, we consider typical organically modified clay particles (as observed by TEM) with a length of 240 nm and a thickness of 6 nm (case 1) and exfoliated individual platelets with a length of 40 nm (case 2) or 240 nm (case 3). For the cases where the particles are individual exfoliated platelets, we assign the particle volume fraction as φ_{MMT} and the particle modulus as 178 GPa. Finally, for comparison, we take the same particle dimensions and volume as case 1, but assign the modulus as 178 GPa (case 4). Fig. 19 shows the model calculations of modulus and CTE for these four cases. A comparison of organically modified clay particles with that of exfoliated platelets at the same aspect ratio of 40 (cases 1 versus 2) shows that the predicted composite modulus (E) is higher for the unexfoliated particles than for the exfoliated platelets even though the modulus of the particles is much higher for the latter. While this may seem counterintuitive, the higher volume fraction of particles (comprised of 40% MMT by volume with a modulus of 70.6 GPa) leads to the greater reinforcement at the same weight percent of MMT and the same aspect ratio. When the aspect ratio increases from 40 to 240 with the particle modulus and volume fraction fixed (cases 2 versus 3), the composite modulus (E) increases as expected. Of course, increasing the modulus of the particles from 70.6 GPa to 178 GPa with the same volume fraction and aspect ratio (cases 1 versus 4) increases the modulus of the composite as seen in Fig. 19(a). These results indicate that the volume fraction of dispersed particles can be more important than the magnitude of the modulus of the particles for modulus enhancements. These trends are in good agreement with the percolation ideas discussed in the rheology section. The predicted trends for CTE are similar to those for modulus (see Fig. 19(b)).

The model calculations described above were based on a constant aspect ratio irrespective of the amount of MMT and did not consider any distribution of aspect ratio from particle to particle. However, the aspect ratios do vary with MMT content and the PP-*g*-MA/organoclay ratio as shown in Fig. 6 and Table 1. Therefore, we now consider the aspect ratio to be a function of MMT content. The values of the aspect ratio for

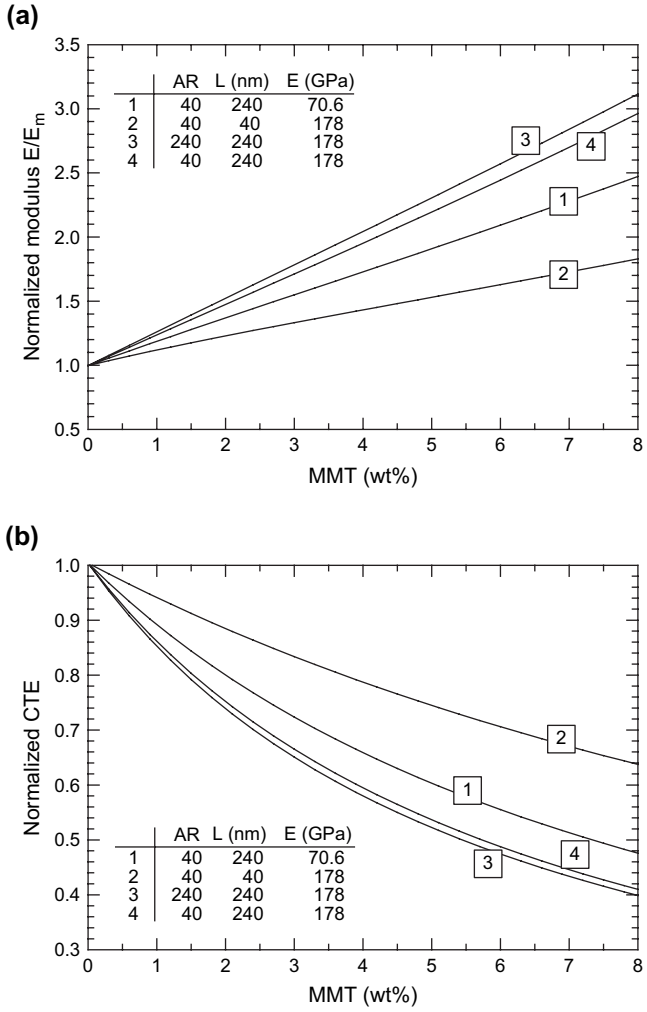

Fig. 19. Prediction of theoretical tensile modulus (a) and linear thermal expansion coefficient (b) considering the aspect ratio, tensile modulus and volume fraction of particles. For these calculations, the MMT content was converted to volume fraction using an MMT density of 2.83 g/cm^3; however, the results are plotted here versus MMT wt% for convenience.

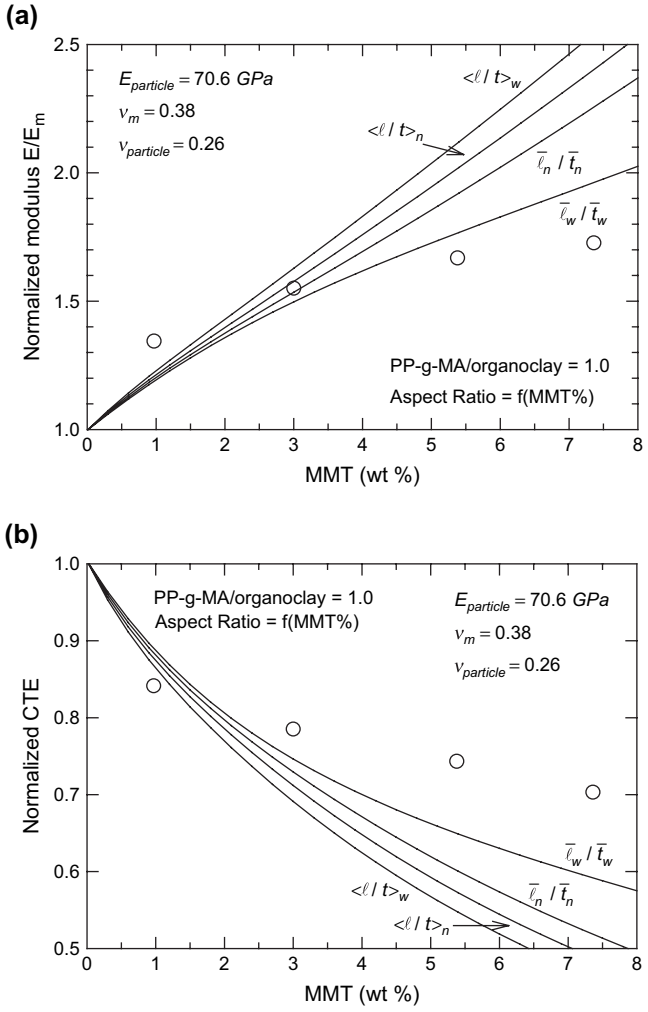

Fig. 20. Prediction of theoretical tensile modulus (a) and linear thermal expansion coefficient (b) by considering the different aspect ratios obtained from TEM observation. For these calculations, the MMT content was converted to volume fraction using an MMT density of 2.83 g/cm^3; however, the results are plotted here versus MMT wt% for convenience.

PP nanocomposites as a function of MMT volume fraction were obtained by regression of the data for $\langle \ell/t \rangle_w$ and $\langle \ell/t \rangle_n$ shown in Fig. 6(b). Similar regression analyses were done for $\bar{\ell}_w/\bar{t}_w$ and $\bar{\ell}_n/\bar{t}_n$ versus MMT content. The magnitude of aspect ratio from TEM is $\langle \ell/t \rangle_w > \langle \ell/t \rangle_n > \bar{\ell}_n/\bar{t}_n > \bar{\ell}_w/\bar{t}_w$. Fig. 20 shows comparisons of the experimental modulus and CTE data with the model predictions considering how each measure of aspect ratios varies with MMT content for a PP-*g*-MA/organoclay ratio of 1.0. Similar results were found for the other ratios of PP-*g*-MA/organoclay. It could be argued that the predicted line based on $\bar{\ell}_w/\bar{t}_w$ seems to provide a better match than other representations of aspect ratio used. However, none of these predictions fully capture the experimental trends. Many factors could contribute to this including the assumption that all particles are perfectly aligned. We believe the volume fraction of particles may be overestimated by considering the intercalated organically modified clay particles as mentioned above causing the model to overestimate the reinforcement. Furthermore, a strictly parallel model for the properties of the particle, as used in Eq. (8), leads to an overestimation of the particle modulus and an underestimation of the particle CTE. A more realistic physical picture of platelet arrangement for incompletely exfoliated particles is suggested in Fig. 5 and in the lower right of Fig. 18. Since the platelets do not run the length of the particle, a parallel model like Eq. (8) may not be justified. Evidence for the latter physical picture is that as the particles become thinner, they also become shorter as discussed earlier (see Fig. 5). The proper average aspect ratio to use when there is a distribution is an interesting problem that can probably be best sorted out by numerical modeling as recently described for the case of a fiber length distribution in composites [48]. Of course, using theories other than that by Chow needs to be considered.

4. Conclusion

The structure–property relationships of PP/PP-*g*-MA/MMT nanocomposites prepared by melt processing have

been investigated with a main focus on the ratio of PP-*g*-MA to organoclay. The morphological observations were used to interpret the mechanical, rheological and thermal properties of these nanocomposites using the Chow model. Detailed morphological studies and subsequent quantitative particle analyses for the dispersed clay phases revealed that the aspect ratio of clay particles decreased as the amount of clay in the nanocomposite increased while it increased as the amount of PP-*g*-MA increased. The rheological properties suggested the extent of a percolation network could be enhanced by increasing the number of stacks at a fixed ratio of PP-*g*-MA to organoclay and by increasing the degree of exfoliation at fixed clay content. However, mechanical and thermal expansion behaviors did not improve correspondingly in all cases because of the reduction of matrix properties by PP-*g*-MA. The reduction of the modulus and the increase in the expansion of the polymer matrix caused by the presence of PP-*g*-MA were accounted for the modeling.

Acknowledgements

The authors thank General Motors for funding this work and the permission to publish it. The authors would like to thank Dr. Douglas Hunter, Dr. P.J. Yoon and Mr. Tony Gonzales of Southern Clay Products for technical assistance and for providing materials. The authors also like to thank Prof. Seung Jong Lee and Prof. Kyung Hyun Ahn of Seoul National University for rheological measurements.

References

[1] Giannelis EP. Adv Mater 1996;8:29.
[2] Alexandre M, Dubois P. Mater Sci Eng 2000;28:1.
[3] Collister J. In: Vaia RA, Krishnamoorti R, editors. Polymer nanocomposites: synthesis, characterization, and modeling. London: Oxford University Press; 2002 [chapter 2].
[4] Ray SS, Okamoto M. Prog Polym Sci 2003;28:1539.
[5] Lui L, Qi Z, Zhu X. J Appl Polym Sci 1999;71(7):1133.
[6] Dennis HR, Hunter DL, Chang D, Kim S, White JL, Cho JW, et al. Polymer 2001;42:9513.
[7] Cho JW, Paul DR. Polymer 2001;42:1083.
[8] Kato M, Usuki A, Okada A. J Appl Polym Sci 1997;66:1781.
[9] Usuki A, Kato M, Okata A, Kurauchi T. J Appl Polym Sci 1997;63:137.
[10] Hasegawa N, Kawasumi M, Kato M, Usuki A, Okada A. J Appl Polym Sci 1998;67:87.
[11] Lele A, Mackley M, Gagali G, Ramesh C. J Rheol 2002;46:1091.
[12] Liu X, Wu Q. Polymer 2001;42:10013.
[13] Marchant D, Jayaraman K. Ind Eng Chem Res 2002;41:6402.
[14] Nam PH, Maiti P, Okamoto M, Kotaba T, Hasegawa N, Usuki A. Polymer 2001;42:9633.
[15] Okamoto M, Nam PH, Maiti P, Kotaka T, Hasegawa N, Usuki A. Nano Lett 2001;1:295.
[16] Reichert P, Nitz H, Klinke S, Brandsch R, Thomann R, Mulhaupt R. Macromol Mater Eng 2000;275:8.
[17] Reichert P, Hoffmann B, Bock T, Thomann R, Mulhaupt R, Friedrich C. Macromol Rapid Commun 2001;22:519.
[18] Kodgire P, Kalgaonkar R, Hambir S, Bulakh N, Jog JP. J Appl Polym Sci 2001;81:1786.
[19] Zang Q, Wang Y, Fu Q. J Polym Sci Part B Polym Phys 2003;41:1.
[20] Gagali G, Ramesh C, Lele A. Macromolecules 2001;34:852.
[21] Garces JM, Moll DJ, Bicerano J, Fibiger R, McLeod DG. Adv Mater 2000;12(23):1835.
[22] Hasegawa N, Okamoto H, Kawasumi M, Kato M, Tsukigase A, Usuki A. Macromol Mater Eng 2000;280/281:76.
[23] Ishida H, Campbell S, Blackwell J. Chem Mater 2000;12(5):1260.
[24] Garcia-Lopez D, Picazo O, Merino JC, Pastor JM. Eur Polym J 2003;39(5):945.
[25] Hasegawa N, Usuki A. J Appl Polym Sci 2004;93(1):464.
[26] Ellis TS, D'Angelo JS. J Appl Polym Sci 2003;90(6):1639.
[27] Fornes TD, Hunter DL, Paul DR. Polymer 2004;45:2321.
[28] Yoon PJ, Fornes TD, Paul DR. Polymer 2002;43:6727.
[29] Chavarria F, Paul DR. Polymer 2004;45:8501.
[30] Lee H-S, Fasulo PD, Rodgers WR, Paul DR. Polymer 2005;46:11673.
[31] Vermogen A, Masenelli-Varlot K, Seguela R, Duchet-Rumeau J, Boucard S, Prele P. Macromolecules 2005;38:9661.
[32] Perrin-Sarazin F, Ton-That MT, Bureau MN, Denault J. Polymer 2005;46:11624.
[33] Morgan AB, Gliman JW. J Appl Polym Sci 2003;87:1329.
[34] Schmidt G, Nakatani AI, Butler PD, Karim A, Han CC. Macromolecules 2000;33:7219.
[35] Ren J, Silver AS, Krishnamoorti R. Macromolecules 2000;33:3739.
[36] Krishnamoorti R, Yurekli K. Curr Opin Colloid Interface Sci 2001;6:464.
[37] Lee H-S, Fasulo PD, Rodgers WR, Paul DR. Polymer 2006;47:3528.
[38] Fornes TD, Paul DR. Polymer 2003;44(17):4993.
[39] Sheng N, Boyce MC, Parks DM, Rutledge GC, Abes JI, Cohen RE. Polymer 2004;45:487.
[40] Chow TS. J Polym Sci Part B Polym Phys 1978;16:959.
[41] Chow TS. J Polym Sci Part B Polym Phys 1978;16:967.
[42] Brune DA, Bicerano JU. Polymer 2002;43:369.
[43] Alexandrov KS, Ryshova TV. Bull Acad Sci USSR Geophys Ser 1961;12:1165.
[44] McNeil LE, Grimsditch M. J Phys Condens Matter 1993;5(1):1681.
[45] Mark JE. Polymer data handbook. Oxford: Oxford University Press; 1999.
[46] Mackinstry HA. Am Mineral 1965;50:212.
[47] Schapery RA. J Comp Mater 1968;2:380.
[48] Hine PJ, Lusti HR, Gusev AA. Compos Sci Technol 2002;62:1445.